Journal of Computational Physics 228 (2009) 1713–1732

Contents lists available at ScienceDirect

Journal of Computational Physics

journal homepage: www.elsevier.com/locate/jcp

High resolution finite volume scheme for the quantum hydrodynamic equations

Chin-Tien Lin [a,*], Jia-Yi Yeh [b], Jiun-Yeu Chen [a]

[a] Department of Applied Internet Science, Hsing Kuo University, Tainan, Taiwan
[b] Department of Management Information Science, Chung Hwa University of Medical Technology, Tainan, Taiwan

ARTICLE INFO

Article history:
Received 7 April 2008
Received in revised form 31 October 2008
Accepted 9 November 2008
Available online 21 November 2008

Keywords:
MOC
Finite volume method
Quantum fluid dynamics
Quantum nanojet

ABSTRACT

The theory of quantum fluid dynamics (QFD) helps nanotechnology engineers to understand the physical effect of quantum forces. Although the governing equations of quantum fluid dynamics and classical fluid mechanics have the same form, there are two numerical simulation problems must be solved in QFD. The first is that the quantum potential term becomes singular and causes a divergence in the numerical simulation when the probability density is very small and close to zero. The second is that the unitarity in the time evolution of the quantum wave packet is significant. Accurate numerical evaluations are critical to the simulations of the flow fields that are generated by various quantum fluid systems.

A finite volume scheme is developed herein to solve the quantum hydrodynamic equations of motion, which significantly improve the accuracy and stability of this method. The QFD equation is numerically implemented within the Eulerian method. A third-order modified Osher–Chakravarthy (MOC) upwind-centered finite volume scheme was constructed for conservation law to evaluate the convective terms, and a second-order central finite volume scheme was used to map the quantum potential field. An explicit Runge–Kutta method is used to perform the time integration to achieve fast convergence of the proposed scheme.

In order to meet the numerical result can conform to the physical phenomenon and avoid numerical divergence happening due to extremely low probability density, the minimum value setting of probability density must exceed zero and smaller than certain value. The optimal value was found in the proposed numerical approach to maintain a converging numerical simulation when the minimum probability density is 10^{-5} to 10^{-12}. The normalization of the wave packet remains close to unity through a long numerical simulation and the deviations from 1.0 is about 10^{-4}.

To check the QFD finite difference numerical computations, one- and two-dimensional particle motions were solved for an Eckart barrier and a downhill ramp barrier, respectively. The results were compared to the solution of the Schrödinger equation, using the same potentials, which was obtained using by a finite difference method. Finally, the new approach was applied to simulate a quantum nanojet system and offer more intact theory in quantum computational fluid dynamics.

1. Introduction

Although the conventional description of quantum mechanical systems uses Schrödinger's equation, an alterative equivalent formalism is quantum fluid dynamics (QFD) [1–11]. In these representations, quantum mechanics is described in terms of a density field and a velocity field, which jointly obey the usual mass and momentum conservation equation

* Corresponding author.
E-mail addresses: ctlin@mail.hku.edu.tw (C.-T. Lin), yeh@mail.hwai.edu.tw (J.-Y. Yeh).

0021-9991/$ - see front matter Crown Copyright © 2008 Published by Elsevier Inc. All rights reserved.
doi:10.1016/j.jcp.2008.11.007

of hydrodynamics for a compressible fluid with a particular constitutive law. The quantum hydrodynamic equations are similar to classical hydrodynamics, except for the presence of an additional term called the ''quantum potential'. The quantum potential couples the quantum trajectories and gives rise to all quantum effects such as tunneling, zero point energy, and interference. This approach is intuitively attractive since the quantum potential and force appear on equal footing with the classical potential and force in the equations of motion.

Despite the intuitively attractive features of this formulation, practical problems arise in implementing a quantum trajectory based approach, due to difficulties in computing an accurate quantum potential. In particular, quantum potential depends on the local curvature of the wave function and can often become singular when nodes form in the wave function or when the wave function is sharply peaked. These inherent properties make an accurate numerical calculation of quantum potential and force very difficult, especially in scattering problems.

The QFD formulation requires solving a set of nonlinear partial differential equations. Classical fluid dynamics can be described in terms of equivalent Eulerian and Lagrangian representations. In recent years, Wyatt et al. [12–14] developed a numerical methodology for solving the deBroglie–Bohm hydrodynamic equations called the quantum trajectory method (QTM) [15,16]. The QTM has been applied to many model problems, including one- and two-dimensional barrier tunneling problems. In this approach, the probability fluid is discretized into fluid elements and the hydrodynamic equations are solved using a Lagrangian frame of reference in which the grid moves with the fluid elements. A moving weighted least squares (MWLS) approach is implemented to calculate the various functions and derivatives that appear in the equations of motion [17–19]. Unfortunately, significant computational problems arise when the QTM is adopted to integrate the hydrodynamic equations of motion. In particular, the interparticle spacings become highly non-uniform with time, such that, some particles move close together and some move far apart. Significant numerical errors accumulate because of the difficulties in evaluating accurate numerical derivatives on a non-uniform grid. Also, the quantum potential is inversely proportional to the magnitude of the wave function and may become singular when the magnitude approaches zero (near nodes). The singularities caused by node formation are usually associated with the interference effects in the reflected part of the wave packet and are most problematic in barrier scattering problems. The singularities cause additional numerical errors which often cause numerical instabilities. A variety of regridding techniques and different frames of reference, such as an arbitrary Lagrangian–Eulerian (ALE) frame, can be adopted the numerical errors and the propagation of the wave packet, and extend the program of the wave packet can to longer times. However, the singularities in the quantum potential eventually cause the numerical calculations to become unstable regardless of frame of reference and the smallness of the interparticle spacings or time steps. An accurate treatment of these interference effects is required to describe many important chemical reaction dynamics processes, including, resonance, and interference effects between the reactive and nonreactive contribution to the cross sections in reactions that involve many identical nuclei. Inelastic scattering also depends on an accurate treatment of the reflected wave packet [20–23].

The direct Euler/Navier–Stokes calculation is widely applied in recent decades to analyze unsteady systems. Many successful methods employ high-order upwind schemes with a flux limiter function to improve numerical stability and obtain more accurate computed results. The inherently dissipative properties of the upwind schemes and limiter functions prevent the generation of the oscillations properties around the discontinuities and therefore promote the capture of the probability density wave. The basis of the finite volume method is that all of the physics must satisfy the principles of conservation law. In the finite volume method, volume integrals in a partial differential equation that contain a divergence term are converted to surface integrals, using the divergence theorem. These terms are then evaluated as fluxes at the surfaces of each finite volume. Since the flux that enters a given volume equals that which leaves the adjacent volume, these methods are conservative.

This study presents a new scheme for solving quantum hydrodynamic equations of motion, which specifically addresses that are the problems associated with the reflected part of the wave packet. A control volume-based technique is used to convert the governing equations into algebraic equations that can be solved numerically and the monotone upwind-centered schemes for conservation laws (MUSCL) method biased TVD scheme (Osher–Chakravarthy scheme) [24,25], based on Roe splitting, [26] is employed to interpolate the changes in the cell properties that occur during the flow simulation. Additionally, the Osher–Chakravarthy (OC) scheme reduces to first-order spatial accuracy at the extreme points, seriously reducing the total accuracy. Therefore, the TVD characteristic of the OS scheme must be modified to obtain better resolution, and a third-order modified Osher–Chakravarthy (MOC) [27] upwind scheme with limiter functions was constructed to evaluate the convective terms, a second-order central finite volume scheme was used to map the field of the quantum potential providing an efficient means of eliminating spurious numerical oscillations, and an explicit Runge–Kutta time integration method [28] for time descritization.

Section 2 derives the relevant set of coupled differential equations. Section 3 discusses the numerical approach in detail. In Section 4, this approach is applied to the scattering of a wave packet from a repulsive external potential barrier and the unitarity of the time evolution of the quantum wave packet is investigated. The accuracy of these results in quantified by comparing them to those based on the Crank-Nicholson algorithm. Section 5 draws conclusions.

2. The Quantum hydrodynamic equations of motion

Let $\psi(\vec{r},t)$ be the wave function representing the state of a one-particle system at any given time t. The wave function is a solution of the Schrödinger equation [29]:

$$ih\frac{\partial\psi}{\partial t}(\vec{r},t) = -\frac{\hbar^2}{2m}\frac{\partial^2\psi}{\partial x^2}(\vec{r},t) + V(\vec{r})\psi(\vec{r},t) \tag{1}$$

$V(\vec{r})$ is the external potential energy surface, and $\vec{r} = (x,y,z)$.

The quantum fluid dynamical formulation of the Schrödinger equation is obtained by expressing the Schrödinger wave function as $\psi(\vec{r},t) = \rho^{1/2}\exp(iS(\vec{r},t)/\hbar)$, where ρ and S are real. Substituting this into the time-dependent Schrödinger equation and separating into the real and imaginary parts, we get a set of coupled difference equations

$$\frac{\partial\rho(\vec{r},t)}{\partial t} + \nabla\cdot\left(\rho\frac{1}{m}\nabla S\right) = 0 \tag{2}$$

$$-\frac{\partial S(\vec{r},t)}{\partial t} = \frac{1}{2m}\mid\nabla S\mid^2 + V(\mathrm{r}) + Q(\vec{r},t) \tag{3}$$

m is the mass. The velocity is defined as $\mathbf{u} = (u,v) = \nabla S/m$. With the exception of the quantum potential these equations are similar to what is found in the classical theory of fluid dynamics. Eq. (2) is recognized as the continuity equation and Eq. (3) is the quantum Hamilton–Jacobi equation expect for the last term involving the quantum potential. All quantum effects are due to the quantum potential

$$Q(\vec{r},t) = \frac{\hbar^2}{2m_e}\left(\frac{\nabla^2\rho^{1/2}}{\rho^{1/2}}\right) = \left(\frac{\hbar^2}{4m_e}\right)\left[\nabla^2(\ln\rho) + \left(\frac{1}{2}\right)\nabla(\ln\rho)\cdot\nabla(\ln\rho)\right] \tag{4}$$

Chiu [6,7] defined the *quantum diffusion velocity* $\mathbf{V_D}$ as

$$\mathbf{V_D} = \frac{\mathbf{J}}{\rho} = -\left(\frac{\hbar}{2m_e}\right)\nabla\ln\rho = -D\frac{\nabla\rho}{\rho} \tag{5}$$

Here $\mathbf{J}$ is the diffusion flux of probability fluid. In this context, the quantity $\hbar/2m_e$ is identified as the quantum diffusion constant D. Note that the first term of the quantum potential is a result of taking divergence of, the quantum diffusion velocity. This term may also be written as,

$$\mathfrak{M} = \left(\frac{\hbar^2}{4m_e}\right)\nabla^2\ln\rho = \left(\frac{\hbar}{2m_e}\right)\left(\frac{\hbar}{2m_e}\right)\nabla\cdot\left(\frac{\nabla\rho}{\rho}\right) = -m_eD\nabla\cdot\mathbf{V_D}. \tag{6}$$

This expression can be interpreted as the work due to quantum dilatational of the diffusion velocity.

Secondly, the quadratic term $(\hbar^2/4m_e)(1/2)\nabla(\ln\rho)\cdot\nabla(\ln\rho)$ represents the kinetic energy associated the quantum diffusive velocity. This can clearly be seen in the following expanded version

$$\mathfrak{K} = \left(\frac{\hbar^2}{4m_e}\right)\left(\frac{1}{2}\right)\nabla(\ln\rho)\cdot\nabla(\ln\rho) = \left(\frac{1}{2}\right)m_e\mathbf{V_D}\cdot\mathbf{V_D} \tag{7}$$

In summary then, the quantum potential consists of a dilatation and a kinetic energy associated with the diffusion of the non-uniform probability density of quantum fluid flow, given by

$$Q(\vec{r},t) = \left(\frac{\hbar^2}{4m_e}\right)\left[\nabla^2(\ln\rho) + \left(\frac{1}{2}\right)\nabla(\ln\rho)\cdot\nabla(\ln\rho)\right] = \mathfrak{M} + \mathfrak{K} = -m_eD\nabla\cdot\mathbf{V_D} + \frac{1}{2}m_e\mathbf{V_D}\cdot\mathbf{V_D} \tag{8}$$

$\mathfrak{M}$ is dilatational energy and $\mathfrak{K}$ is quantum kinetic energy. The quantum potential $Q(\vec{r},t)$ can also be expressed in the following two alternative forms. All the expressions of the quantum potential are equivalent to each other.

$$Q_{\rho/2} = \frac{\hbar^2}{2m_e}\left(\frac{\nabla^2\rho^{1/2}}{\rho^{1/2}}\right) = Q_\rho = \frac{\hbar^2}{4m_e}\left(\frac{\nabla^2\rho}{\rho} - \frac{1}{2}\frac{\nabla\rho\cdot\nabla\rho}{\rho^2}\right) \tag{9}$$

Thus the same and similar numerical methods may be employed as used in classical computational fluid dynamics.

3. Numerical formulations

This work presents finite volume method for simulating quantum hydrodynamic equations of motion, while dealing with the problems associated with the reflected part of the wave packet, as described below.

3.1. Governing equations of quantum hydrodynamics

The numerical schemes discussed are based on the MUSCL type. Rewrite Eqs. (2) and (3) in integral form as

$$\frac{\partial}{\partial t}\iiint_\Omega W d\Omega + \int\int_\Gamma (F,G)\cdot\vec{n}d\Gamma = \iiint_\Omega H d\Omega \tag{10}$$

where

$$W=\begin{pmatrix}\rho\\ \rho u\\ \rho v\end{pmatrix},\quad F=\begin{pmatrix}\rho\\ \rho u^2\\ \rho uv\end{pmatrix},\quad G=\begin{pmatrix}\rho\\ \rho uv\\ \rho v^2\end{pmatrix},\quad H=2\rho\begin{pmatrix}0\\ Q_x\\ Q_y\end{pmatrix}$$

In which Ω is the control volume, Γ is the boundary of V and $\vec{n}$ is the outer unit normal. The $d\Gamma$ is the surface area of the control volume. W represents the vector of conservation variables. The second term in the left-hand side of the Eq. (10) is the flux vector and the right-hand side of the Eq. (10) is the quantum flux vector.

3.2. Space discretization: finite volume formulation

3.2.1. Treatment of convection terms

The computation procedure starts by discretizing the domain of interest into quadrilaterals labeled as K_{ij}. The subscripts i and j label the direction. In each hexahedron K_{ij}, flow variables are stored at the barycenter C_{ij} and the flow conservation is enforced on the boundary surface ∂K_{ij}. In this section, assume that the grid mesh is geometrically time invariant and the flow variables stored at the barycenter C_{ij} are a volume average of the integrated flow variables in the hexahedron K_{ij}. Flow variables are then computed at the barycenter of each quadrilateral. The solutions at the boundaries of the quadrilaterals are matched up imposing the flow conservation of convective terms across the boundaries. A third-order upwind finite volume method is used for the convection terms and the central finite difference method is used for the quantum potential terms. Then in each quadrilateral, K_{ij}, Eqs. (2) and (3) can be written as

$$\frac{dW_{ij}}{dt}=-\frac{1}{A_{ij}}\oint_{\Gamma_{ij}}(F,G)\cdot ndl-H_{ij} \tag{11}$$

where A_{ij} is the area of K_{ij}, and $\Gamma_{ij}=\partial K_{ij}$

To evaluate the first term of the right-hand side of Eq. (11), we sum all the flux vectors on the four edges of

$$\oint_{\Gamma}(F,G)\cdot ndl\sim h_{i-1/2,j}\mid e_{i-1/2,j}\mid+h_{i+1/2,j}\mid e_{i+1/2,j}\mid+h_{ij-1/2}\mid e_{ij-1/2}\mid+h_{ij+1/2}\mid e_{ij+1/2}\mid \tag{12}$$

Here $h_{i+1/2,j}$ is the numerical approximation for the flux associated with the edge $e_{i+1/2,j}$ and $|e_{i+1/2,j}|$ is the length of the edge $e_{i+1/2,j}$. In order to evaluate $h_{i+1/2,j}$ using an upwind scheme, it is necessary to have two fluid dynamic states, $W^R_{i+1/2,j}$ and $W^L_{i+1/2,j}$. They are interpolated from the cell-centered states by means of the third-order monotonic upstream schemes for conservation laws (MUSCL) scheme [24,25]. They can be expressed as

$$W^R_{i+1/2,j}=W_{i+1,j}-a_{i+1,j}\left[(c_{i+1,j}-2\kappa b_{i+1,j})(W_{i+2,j}-W_{i+1,j})+\frac{1}{c_{i+1,j}}(1+2\kappa b_{i+1,j})(W_{i+1,j}-W_{ij})\right] \tag{13}$$

and

$$W^L_{i+1/2,j}=W_{ij}+a_{ij}\left[(c_{ij}-2\kappa b_{ij})(W_{ij}-W_{i-1,j})+\frac{1}{c_{ij}}(1+2\kappa b_{ij})(W_{i+1,j}-W_{ij})\right] \tag{14}$$

where the non-uniformity of cell sizes is taken into account in $a_{i,j}$, $b_{i,j}$, $c_{i,j}$. Let $l_{i,j}$ represent the width of cell $K_{i,j}$ in the i direction; then

$$\begin{aligned}a_{ij}&=\frac{l_{ij}}{l_{i+1,j}+2l_{ij}+l_{i-1,j}}\\ b_{ij}&=\frac{l_{ij}}{l_{ij}+l_{i+1,j}}\\ c_{ij}&=\frac{l_{ij}+l_{i-1,j}}{l_{ij}+l_{i+1,j}}\end{aligned} \tag{15}$$

for a uniform mesh, they become

$$a_{ij}=\frac{1}{4},\quad b_{ij}=\frac{1}{2},\quad c_{ij}=1$$

Eqs. (13) and (14) reduces to the standard form described by Osher and Chakravarthy [25], then Eqs. (13) and (14) becomes

$$W^R_{i+1/2,j}=W_{i+1,j}-\frac{1}{4}\left[(1+\kappa)(W_{i+1,j}-W_{ij})+(1-\kappa)(W_{i+2,j}-W_{i+1,j})\right] \tag{16}$$

$$W^L_{i+1/2,j}=W_{ij}+\frac{1}{4}\left[(1+\kappa)(W_{i+1,j}-W_{ij})+(1-\kappa)(W_{ij}-W_{i-1,j})\right] \tag{17}$$

The value of κ determines the type of difference scheme: $\kappa=-1$ yields a one-sided upwind scheme; $\kappa=1$ yields a central difference scheme. The spatial accuracy at local extrema is first-order. Away from the local extrema and steep gradients,

the interpolation polynomials of Eqs. (16) and (17) yields a scheme of third-order spatial accuracy for $\kappa = 1/3$. To capture the singularities of the probability density precisely, the computation must by performance using a high-order accuracy scheme. In this study, $\kappa = 1/3$ is used. This TVD scheme is formally third-order in space with $\kappa = 1/3$ away from the local extrema.

However, a number of numerical singularities exist at certain critical points. The OC (Osher and Chakravarthy) scheme reduces to first-order spatial accuracy at those extreme points, and significantly reducing the total accuracy. Therefore the TVD characteristic of the OC scheme needs to be modified to improve resolution.

In this scheme W^R and W^L obtained in Eqs. (16) and (17) are stabilized using a local projection limiter

$$W^{R,m}_{i+1/2,j} = W_{i+1,j} - \min\ \mathrm{mod}(W_{i+1,j} - W^R_{i,j}, \Delta_{i+1/2}W_{i,j}, \Delta_{i+1/2}W_{i+1,j}) \tag{18}$$

$$W^{L,m}_{i+1/2,j} = W_{i,j} + \min\ \mathrm{mod}(W^L_{i+1/2} - W_{i,j}, \Delta_{i+1/2}W_{i,j}, \Delta_{i+1/2}W_{i-1,j}) \tag{19}$$

Here

$$\min\ \mathrm{mod}(a,b,c) = \begin{cases} \min(a,b,c) & a,b,c \geqslant 0 \\ \max(a,b,c) & a,b,c \leqslant 0 \\ 0, & \text{otherwise} \end{cases} \tag{20}$$

$$\Delta_{i+1/2}W_{i,j} = W_{i+1,j} - W_{i,j}$$

Similarity, for $W^L_{i,j+1/2}$ and $W^R_{i,j+1/2}$ at the edge $e_{i,j+1/2}$. Then the numerical flux at the interface is written as

$$\begin{aligned} h_{i+1/2,j} &= h\left(W^L_{i+1/2}, W^R_{i+1/2}\right) \\ &= \frac{1}{2}\left[\left(F\left(W^L_{i+1/2,j}\right) + F\left(W^R_{i+1/2,j}\right)\right)\cdot n_x + \left(G\left(W^L_{i+1/2,j}\right) + G\left(W^R_{i+1/2,j}\right)\right)\cdot n_y - \alpha_{i+1/2,j}\cdot\left(W^R_{i+1/2,j} - W^L_{i+1/2,j}\right)\right] \end{aligned} \tag{21}$$

Here, the local Lax–Friedrichs monotone method is used to define the value $\alpha_{i+1/2,j}$ as:

$$\begin{aligned} &\alpha_{i+1/2,j} = \max(|\ U^L_n\ |, |\ U^R_n\ |, \varepsilon) \\ &\varepsilon = 0.01 \sim 0.001 \end{aligned} \tag{22}$$

Here $U_n = u_{i+1/2,j}\cdot n_x + v_{i+1/2,j}\cdot n_y$ is the contravariant velocity normal to the edge $e_{i+1/2,j}$.

Theoretically, the Modified Osher and Chakravarthy scheme (MOC scheme) is very similar to the OC scheme. However, the MOC scheme is simpler and yielded better numerical results herein than the OC scheme.

3.2.2. Treatment of quantum terms

The central finite difference method is used to evaluate the quantum potential term. For simplicity, the formula in the Cartesian grid is

$$\nabla^2 f = \frac{f_{i+1,j} - 2f_{i,j} + f_{i-1,j}}{\Delta x^2} + \frac{f_{i,j+1} - 2f_{i,j} + f_{i,j-1}}{\Delta y^2} \tag{23}$$

$$f_x = \frac{f_{i+1,j} - f_{i-1,j}}{2\Delta x}, \quad f_y = \frac{f_{i,j+1} - f_{i,j-1}}{2\Delta y} \tag{24}$$

3.3. Time integration: Runge–Kutta time integration

An explicit two-order Runge–Kutta time integration [28] is used to discretize the remaining time derivative in Eq. (11). We define the residual as:

$$\mathrm{Res}_{ij} = -\frac{1}{A_{ij}}\oint (F,G)\cdot ndl - H_{ij} \tag{25}$$

Then, Eq. (10) becomes

$$\frac{dW_{ij}}{dt} = \mathrm{Res}_{ij} \tag{26}$$

The two-order Runge–Kutta time integration is as follows:

$$W^{(0)}_{ij} = W^n_{ij} \tag{27a}$$

$$W^{(1)}_{ij} = W^{(0)}_{ij} + \Delta t\mathrm{Res}_{ij}(W^{(0)}) \tag{27b}$$

$$W^{(2)}_{ij} = W^{(1)}_{ij} + \Delta t\mathrm{Res}_{ij}(W^{(1)}) \tag{27c}$$

$$W^{(n+1)}_{ij} = 0.5(W^{(0)}_{ij} + W^{(2)}_{ij}) \tag{27d}$$

we define

$$CFL_{i,j} = \frac{\Delta t_{i,j} C_{\max}}{|e_{i,j}|_{\min}} \tag{28}$$

where $|e_{i,j}|_{\min} = \min(|e_{i+1/2,j}|, |e_{i-1/2,j}|, |e_{i,j+1/2}|, |e_{i,j-1/2}|)$, and

$$C_{i+1/2,j} = \max\left(\sqrt{[(U_n^L)^2 + \beta]}, \sqrt{[(U_n^R)^2 + \beta]}\right),$$
$$U_n = u_{i+1/2,j} \cdot n_x + v_{i+1/2,j} \cdot n_y$$
$$C_{\max} = \max(C_{i+1/2,j}, C_{i-1/2,j}, C_{i,j+1/2}, C_{i,j-1/2}) \tag{29}$$

At this moment, the entire scheme is stable for Courant number $CFL_{i,j} \leqslant 1$.

In the following section, validations are presented to evaluate the accuracy of the flow solver that was described in the preceding section. To demonstrate the capability of the present solver to capture one- and two- dimensional particle

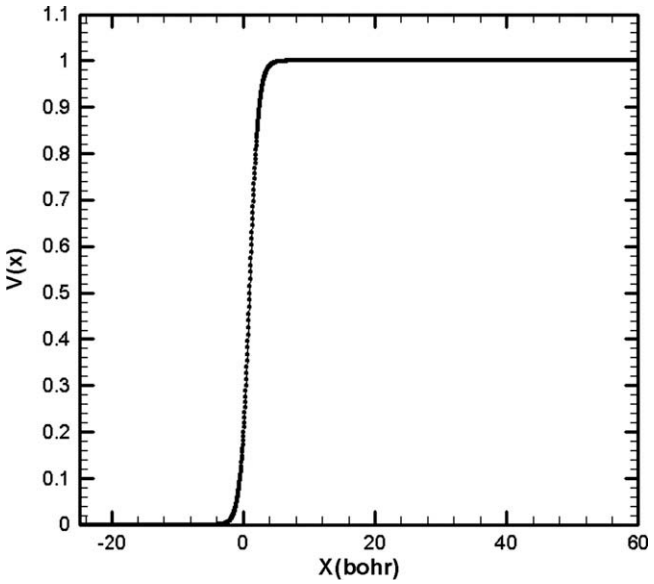

Fig. 1. Eckart potential distribution.

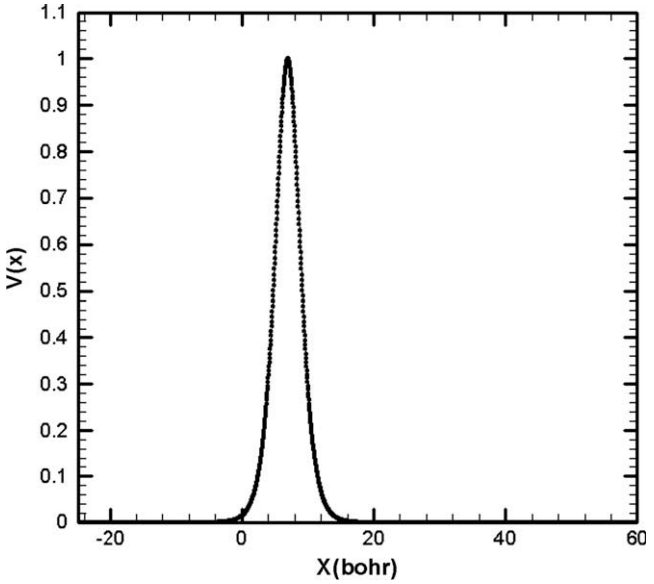

Fig. 2. Downhill ramp potential distribution.

motions, the numerical results in each case in which an external potential is present, are compared with those obtained by directly solving the Schrödinger equation.

3.4. Boundary condition

Several boundary conditions are given as following. The flow filed is similar to external flow, so the far field boundary condition is needed. The probability density and velocity is interpolated from the computational domain. The other probability density and velocity are given.

4. Applications

A. External potential barrier and unitarity

In the section, we will consider the scattering of a one-dimensional Gaussian wave packet from a repulsive Eckart barrier and downhill ramp barrier.

The Eckart potential (Fig. 1) is given by

$$V(x) = V_0 V_P(x) = V_0 sech^2[a(x - x_b)] \tag{30}$$

The other external potential is downhill ramp potential (Fig. 2) as follow

$$V(x) = V_0 \frac{1}{1 + e^{-2.5(x-1.0)}} \tag{31}$$

where V_0 is the barrier height, $a = 0.4$ determines the width, and x_b is the location of the barrier maximum. The mass used in the calculations is $m = 2000$ a.u. The initial Gaussian wave packet at $t = 0$ is given by

$$\psi(x, 0) = \left(\frac{2\beta}{\pi}\right)^{1/4} e^{-\beta(x-x_0)^2} e^{ik(x-x_0)} \tag{32}$$

Table 1
Parameters for 1D wave packet motion with Eckart potential.

V_0 (barrier height)	0.992 (eV)
β	$4a_0^{-2}$ (a_0 is Bohr radius)
Energy	0.8 (eV)
m (mass)	2000 (a.u), 1 (a.u) = 9.109×10^{-31} kg
x_0 (initial wave packet center)	$2.0a_0$
x_b (the location of the barrier maximum)	$7.0a_0$
u_0 (initial velocity)	0.00542626
dx	0.03
dt	0.05

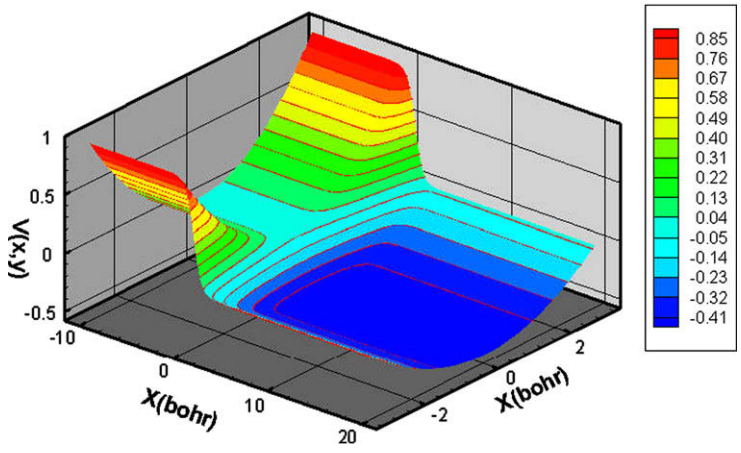

Fig. 3. A mesh-contour plot of 2D downhill ramp potential.

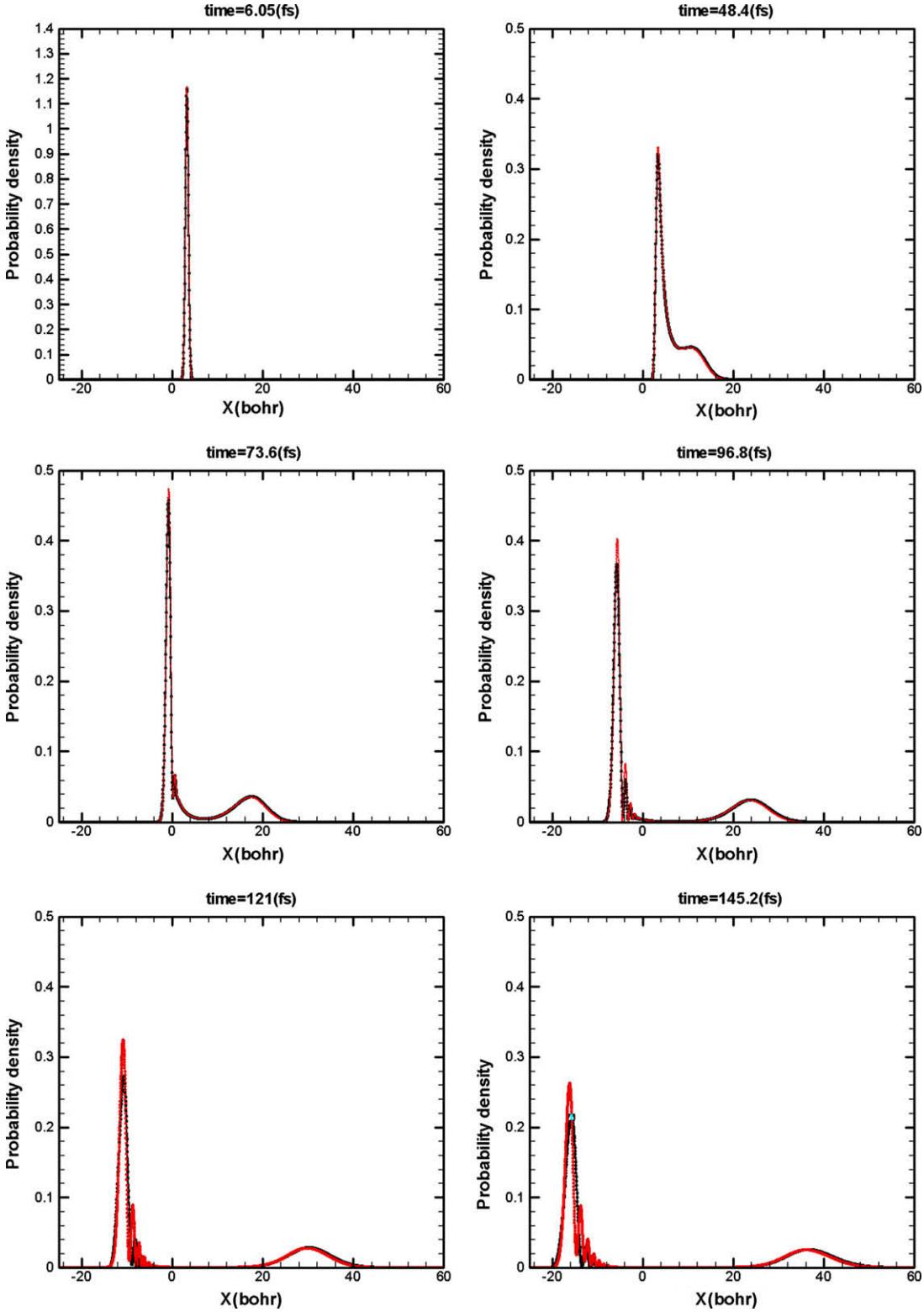

Fig. 4. Probability density of free particle that is moving under Eckart potential at several time steps for $E = 0.8$ eV. The red lines represent the numerical solution of Schrödinger equation and black lines represent numerical solution using the QFD formulation. (For interpretation of the references in colour in this figure legend, the reader is referred to the web version of this article.)

where β is the width parameter, x_0 is the center of the wave packet, and k determines the initial phase $S_0 = \hbar k(x - x_0)$ and flow kinetic energy $E = \hbar^2 k^2/(2m)$. The initial conditions for the velocity are give by $u_0 = (1/m)\partial S_0/\partial x = \hbar k/m$. The one dimension Schrödinger equation including the external potential is

$$i\hbar\frac{\partial\psi}{\partial t} = -\frac{\hbar^2}{2m}\frac{\partial^2\psi}{\partial x^2} + V_0 V_p(x)\psi \tag{33}$$

We select the following reference quantities as characteristic quantities of interest

$$\bar{x} = \frac{x}{a_0}, \quad \bar{y} = \frac{y}{a_0}, \quad \tau = \frac{t}{T_0}, \quad \bar{u} = \frac{u}{U}, \quad \bar{v} = \frac{v}{U}, \quad U = \frac{a_0}{T_0}$$

where T_0 is a characteristic time, a_0 is the Bohr radius, U is the characteristic velocity.

With the above, the time-dependent Schrödinger equation may be written in a non-dimensional form as

$$i\frac{\partial\psi}{\partial\tau} = -\frac{T_0\hbar}{2m}\frac{1}{a_0^2}\frac{\partial^2\psi}{\partial\bar{x}^2} + \frac{T_0 V_0}{\hbar}V_p(\bar{x})\psi \tag{34}$$

The fluid dynamics formulation for this one dimension problem is

$$\frac{\partial\rho}{\partial\tau} + \frac{\partial(\rho\bar{u})}{\partial\bar{x}} = 0 \tag{35}$$

$$\frac{\partial\rho\bar{u}}{\partial\tau} + \frac{\partial(\rho\bar{u}^2)}{\partial\bar{x}} - \frac{\hbar^2}{2m_a^2 a_0^2 u_c^2}\rho\frac{\partial}{\partial\bar{x}}\left[\rho^{-1/2}\frac{\partial^2\rho^{1/2}}{\partial\bar{x}^2}\right] + \frac{1}{mu_c^2}\rho\frac{\partial}{\partial\bar{x}}V_p(\bar{x}) = 0 \tag{36}$$

The initial wave packet parameters for the Eckart potential model are listed in Table 1.

Fig. 4 plots the time evolution of the amplitude of wave packet scattering from an Eacker potential ($E = 0.8$ eV) at times 6.05, 48.4, 73.6, 96.8, 121, and 145.2 (fs). As the wave packet moves to the right, it scatters from the Eckart barrier centered at $r = 7a_0$. At $t = 48.5$ fs the wave packet is tunneling through the barrier and is beginning to split into a transmitted part and a reflected part. At 73.6 fs, the splitting is nearly complete and the split wave packets are moving to the right and left. Interference effects become evident in the reflected part of the wave packet. The transmitted part of the wave packet is "Gaussian-type." At $t = 96.8$ fs, the interference effects have become more pronounced than before and a series of ripples have formed behind the mail peak of the reflected wave packet. The transmitted and reflected parts of the wave packet continue to move apart and broaden in interval of 121 fs and 145 fs, respectively. The calculations are quite stable and were made until $t = 220$ fs.

Table 2 presents the initial values of the wave packet parameters for use in the downhill ramp potential model. Fig. 5 plots the time evolution of the amplitude of the wave packet that is scattered from an downhill ramp potential ($E = 0.8$ eV) at times 6.05, 48.4, 73.6, 96.8, 121, and 145.2 (fs). The presented solution agrees well with the Crank–Nicholson results, the results of this study capture all of the oscillations in the wave function.

The probability of finding a particle somewhere in a given region must be unity at all times. This condition demands the proper normalization of the wave packet at all times [29]. Quantum hydrodynamic solutions must ultimately satisfy the Schrödinger equation and thus must also be properly normalized. A difficulty arises because the solutions to the (quantum) hydrodynamic equations are not analytic but numerical. Therefore, an exact normalized solution is out of the question. A convergent solution of some kind is most favorable possibility. Limitations on the accuracy of numerical solutions are inherent in any calculation because of the accuracy of the machine, error build-up by propagation through multiple iterations, due to truncation and round off, and the accuracy of the numerical method. However, if the initial wave packet is normalized properly, then periodic checks to track the normalization as time evolves can effectively yield the accuracy of the calculation.

Fig. 6 plots the normalization of the wave packet for $E = 0.8$ eV in the MOC approach using the methodology discussed in Section 3. A grid spacing of $\Delta x = 0.03a_0$ was used. The normalization of the wave packet at each time step is computed using $\text{Norm} = \int_{r_1}^{r_N} |\psi(x,t)|^2 dx$ and a Romberg integration scheme. The normalization of the wave packet remains close to unity through the propagation and the deviations from 1.0 are always smaller less than 3×10^{-4}.

Table 2
Parameters for 1D wave packet motion with downhill ramp potential.

V_0 (barrier height)	0.992 (eV)
β	$4a_0^{-2}$ (a_0 is Bohr radius)
Energy	0.8 (eV)
m (mass)	2000 (a.u), 1 (a.u) = 9.109×10^{-31} kg
x_0 (initial wave packet center)	$0.0a_0$
u_0 (initial velocity)	0.00542626
dx	0.03
dt	0.05

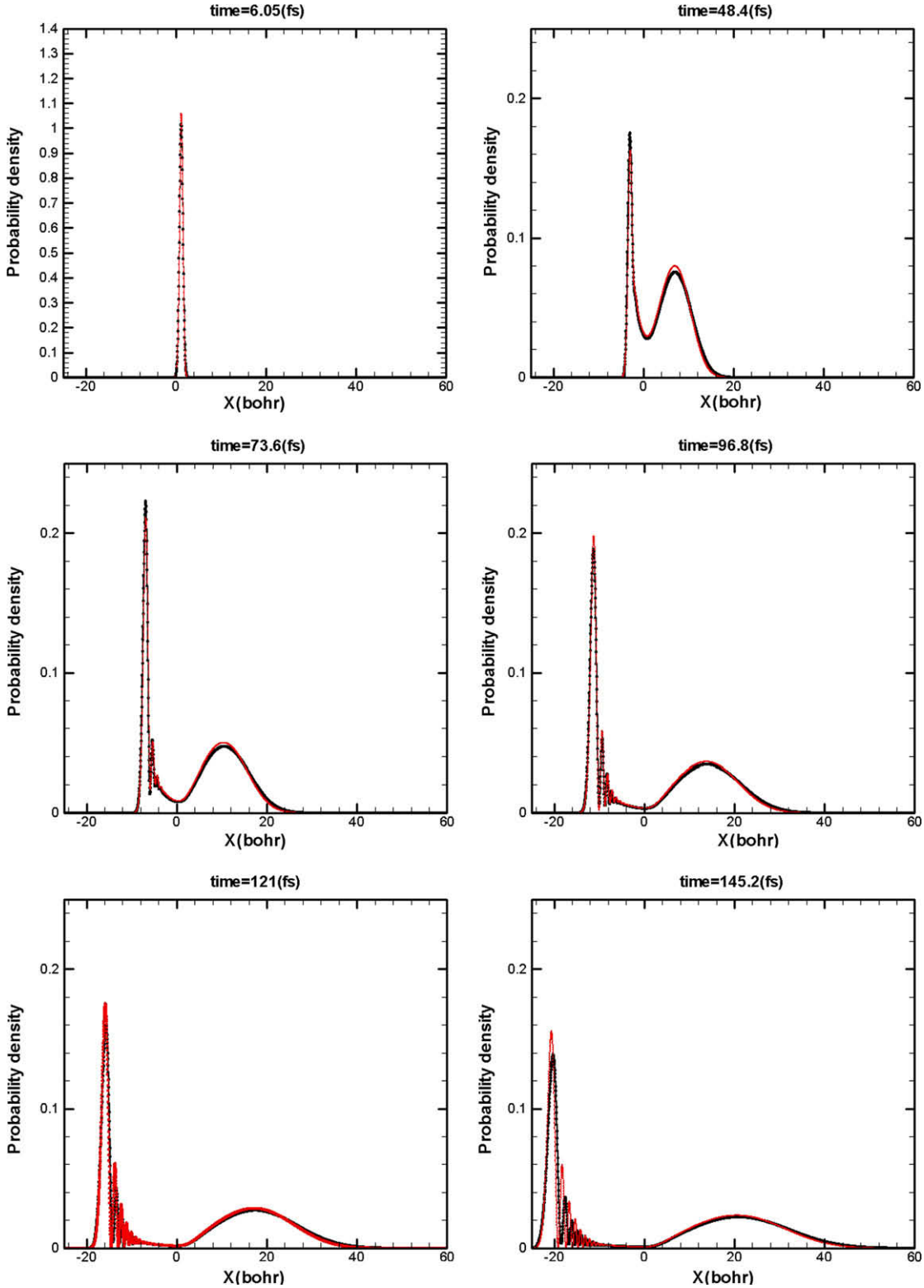

Fig. 5. Probability density of free particle in motion under downhill ramp potential at several time steps for $E = 0.8$ eV. The red lines represent the numerical solution to the Schrödinger equation and black lines represent the numerical solution using the QFD formulation. (For interpretation of the references in colour in this figure legend, the reader is referred to the web version of this article.)

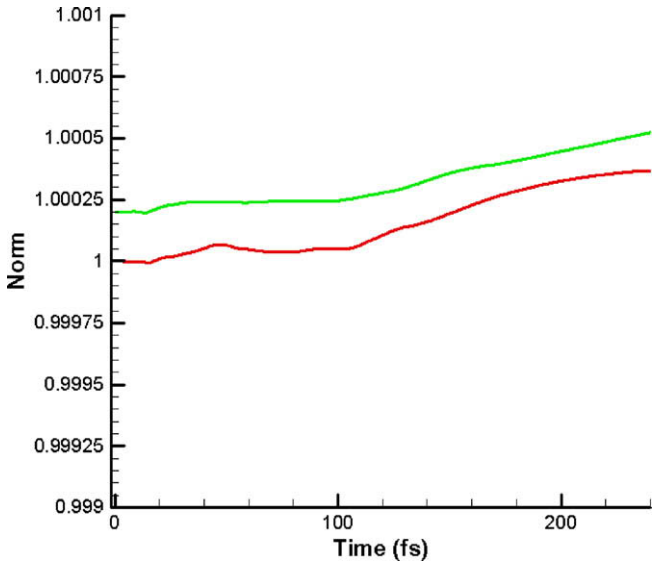

Fig. 6. Normalization of wave packet under Eckart potential (red line) and downhill ramp potential (green line) as function of time for $E = 0.8$ eV in the MOC approach. (For interpretation of the references in colour in this figure legend, the reader is referred to the web version of this article.)

Table 3
Parameters for 2D wave packet motion with downhill ramp potential.

V_1	-0.5
V_2	0.01
β_x	$8a_0^{-2}$ (a_0 is Bohr radius)
β_y	$8a_0^{-2}$
Energy	0.8 (eV)
m (mass)	2000 (a.u) 1 (a.u) = 9.109×10^{-31} kg
(x_0,y_0) (initial wave packet center)	(0,0)
x_b (the location of the barrier maximum)	$7.0a_0$
u_0 (initial velocity)	0.00542626
v_0 (initial velocity)	0
dx	0.03
dy	0.03
dt	0.05

B. Two-dimensional particle motion in downhill ramp potential

The application in this section is the propagation of a 2D Gaussian wave packet under the downhill ramp potential is given by

$$V(x,y) = \frac{V_1}{1+e^{-2.5(x-1)}} + \frac{1}{2}V_2 y^2\left(\frac{2}{1+e^{2.5(x-1)}} + \frac{2}{1+e^{-2.5(x-1)}}\right) \tag{37}$$

In Fig. 3, $V_1 < 0$ and $V_2 > 0$. This potential, for example, may represent the relaxation of a molecule's vibration during an exothermic reaction. Two-dimensional potentials are generally not separable in coordinates, so the resulting Schrödinger equation is also not separable. The downhill ramp potential in Eq. (32) provides an example of this inseparability. Since the Schrödinger equation is not separable, it has no analytic solution, and numerical methods must be adopted.

Table 3 specifies the initial condition used in the simulation.

The two-dimensional Schrödinger equation including the downhill ramp potential is

$$i\hbar\frac{\partial\psi(x,y)}{\partial t} = -\frac{\hbar^2}{2m}\left(\frac{\partial^2\psi}{\partial x^2} + \frac{\partial^2\psi}{\partial y^2}\right) + V\psi(x,y) \tag{38}$$

Converting this to a non-dimensional form results in

$$i\frac{\partial\psi}{\partial\tau} = -\frac{T_0\hbar}{2m}\frac{1}{a_0^2}\left(\frac{\partial^2\psi}{\partial\bar{x}^2} + \frac{\partial^2\psi}{\partial\bar{y}^2}\right) + \frac{T_0}{\hbar}\left[\frac{V_1}{(1+\exp^{-1.5(\bar{x}-1.0)})} + \frac{1}{2}V_2\bar{y}^2\left(\frac{2}{(1+\exp^{2.5(\bar{x}-1.0)})} + \frac{1}{(1+\exp^{-2.5(\bar{x}-1.0)})}\right)\right]\psi \tag{39}$$

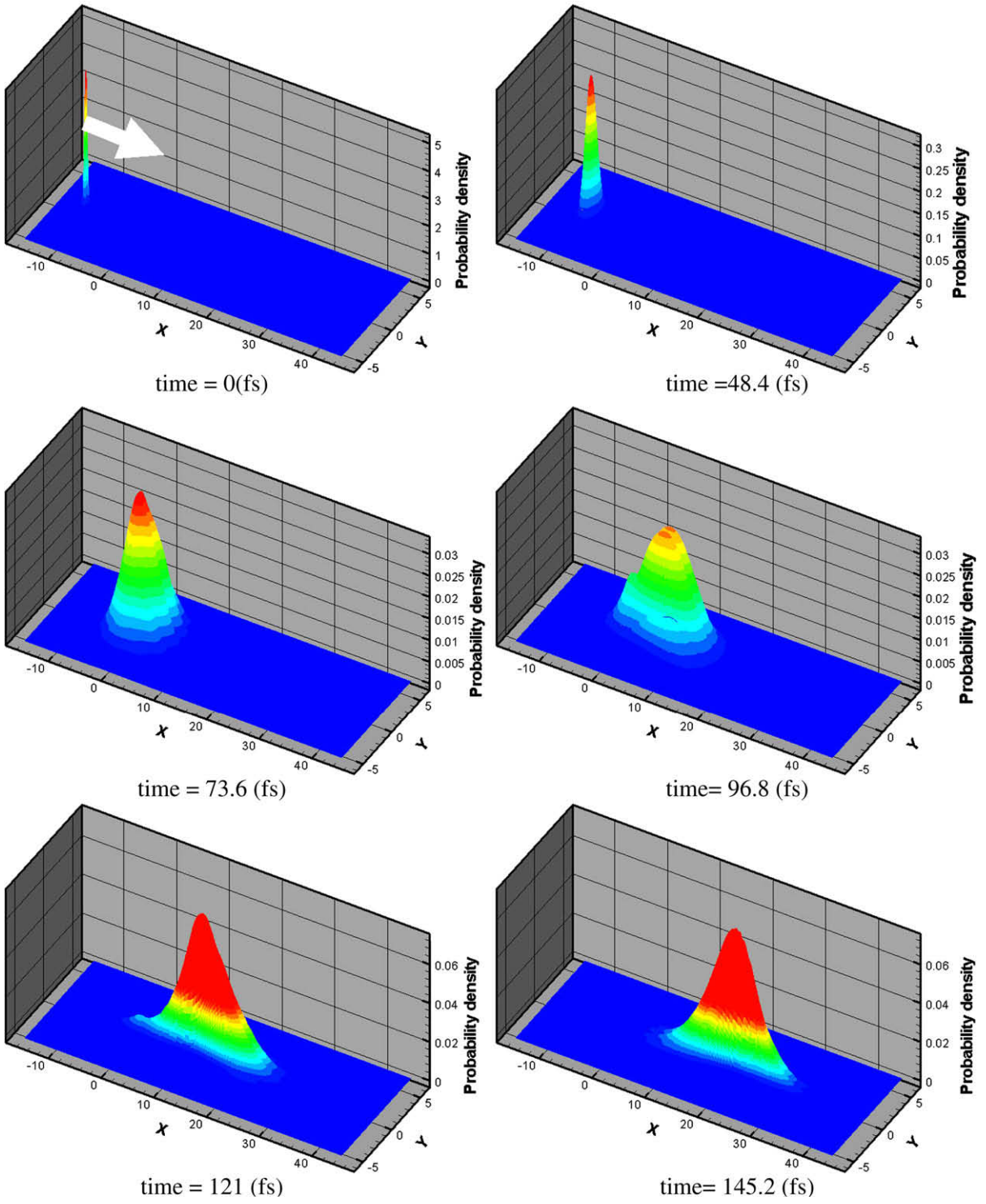

Fig. 7. Probability density of wave packet in motion under 2D downhill ramp potential at several time steps for $E = 0.8$ eV. Initial velocity $u_0 = 0.005424$.

The corresponding continuity and x-component momentum equations, written in fluid dynamics formulation are, respectively,

$$\frac{\partial \rho}{\partial \tau} + \frac{\partial \rho \bar{u}}{\partial \bar{x}} + \frac{\partial \rho \bar{v}}{\partial \bar{y}} = 0 \tag{40}$$

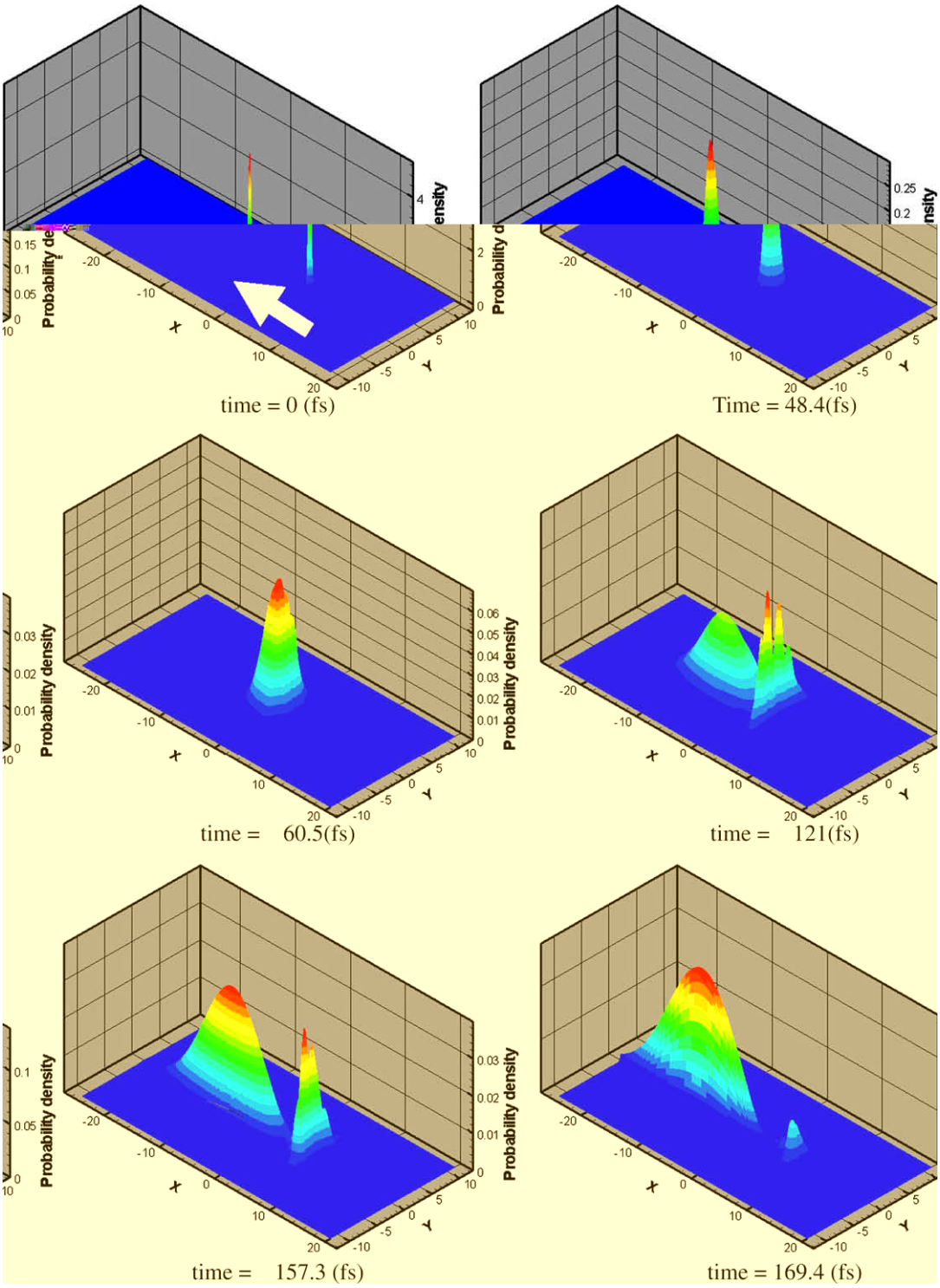

Fig. 8. Probability density of wave packet in motion under 2D downhill ramp potential at several time steps for $E = 0.8$ eV. Initial velocity $u_0 = -0.005424$.

$$\frac{\partial \rho \bar{u}}{\partial \tau} + \frac{\partial (\rho \bar{u}^2)}{\partial \bar{x}} + \frac{\partial (\rho \bar{u}\bar{v})}{\partial \bar{y}} - \frac{\hbar^2}{2m_a^2 a_0^2 u_c^2} \rho \frac{\partial}{\partial \bar{x}} \left[\rho^{-1/2} \left(\frac{\partial^2 \rho^{1/2}}{\partial \bar{x}^2} + \frac{\partial^2 \rho^{1/2}}{\partial \bar{y}^2} \right) \right] + \frac{1}{m u_c^2} \rho \frac{\partial}{\partial \bar{x}} \left[\frac{V_1}{(1 + \exp^{-1.5(\bar{x}-1.0)})} + \frac{1}{2} V_2 \bar{y}^2 \left(\frac{2}{(1 + \exp^{2.5(\bar{x}-1.0)})} + \frac{1}{(1 + \exp^{-2.5(\bar{x}-1.0)})} \right) \right] = 0 \tag{41}$$

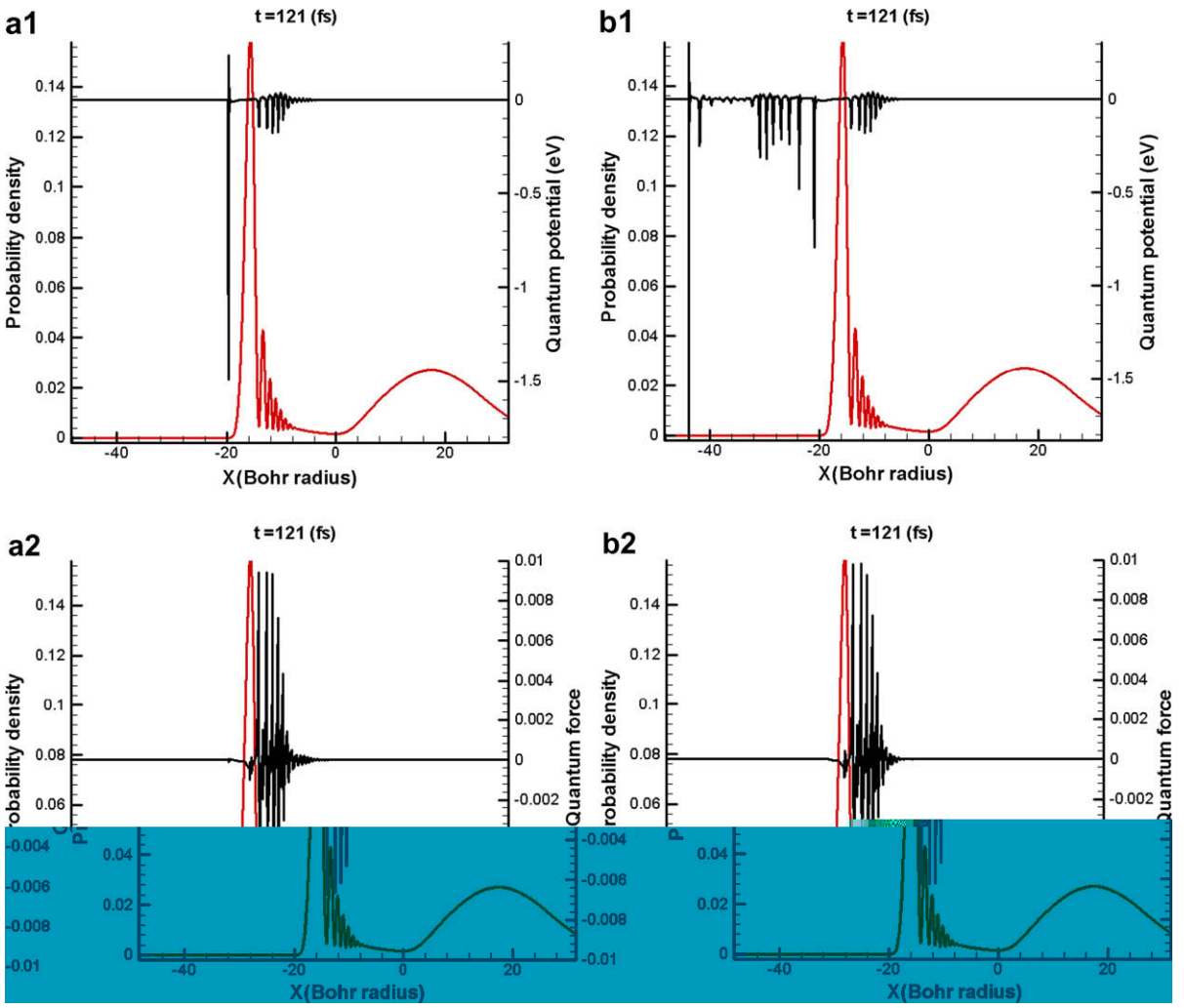

Fig. 9. The amplitude of probability density and the quantum force obtained from the minimum setup probability density using the numerical simulation. (a) $\rho = 10^{-5}$ and (b) $\rho = 10^{-12}$ 1D wave packet motion with Eckart potential at time = 121(fs).

The y-component momentum equation is

$$\frac{\partial \rho \bar{v}}{\partial \tau} + \frac{\partial (\rho \bar{u} \bar{v})}{\partial \bar{x}} + \frac{\partial (\rho \bar{v}^2)}{\partial \bar{y}} - \frac{\hbar^2}{2 m_a^2 a_0^2 u_c^2} \rho \frac{\partial}{\partial \bar{y}} \left[\rho^{-1/2} \left(\frac{\partial^2 \rho^{1/2}}{\partial \bar{x}^2} + \frac{\partial^2 \rho^{1/2}}{\partial \bar{y}^2} \right) \right] + \frac{1}{m u_c^2} \rho \frac{\partial}{\partial \bar{y}} \left[\frac{V_1}{(1 + \exp^{-1.5(\bar{x}-1.0)})} + \frac{1}{2} V_2 \bar{y}^2 \left(\frac{2}{(1 + \exp^{2.5(\bar{x}-1.0)})} + \frac{1}{(1 + \exp^{-2.5(\bar{x}-1.0)})} \right) \right] = 0 \tag{42}$$

Fig. 7 plots the time-development of the QFD formulation in the downhill ramp potential with the initial velocity in the positive x-direction, and Fig. 8 plots the time-development with the initial velocity in the negative x-direction.

Another interesting feature of the quantum flow fields in the presence of the singularities at the position of the vanishing wave function or density probability density, is the divergence of both dilatation and diffusion kinetic energy, which phenomenon is similar to that associated with the expansion of the fluid to the vacuum state in classical fluid flow. A force pushes a wave forward in a quantum potential force, as numerically simulated waves pass through external potential energies, in the area of approximately zero probability density, the quantum potential variation increases, causing calculation errors in the quantum hydrodynamic simulations. Hence, in the numerical simulation, to maintain the calculation accuracy, the minimum probability density must be set, although this setting dominates the accuracy of the simulation and, as the simulation time increases, the accumulated errors become unable to converge. This work, discusses the effect of the singularity. Fig. 9 present the results of the amplitude probability density and quantum potential force obtained from the mini-

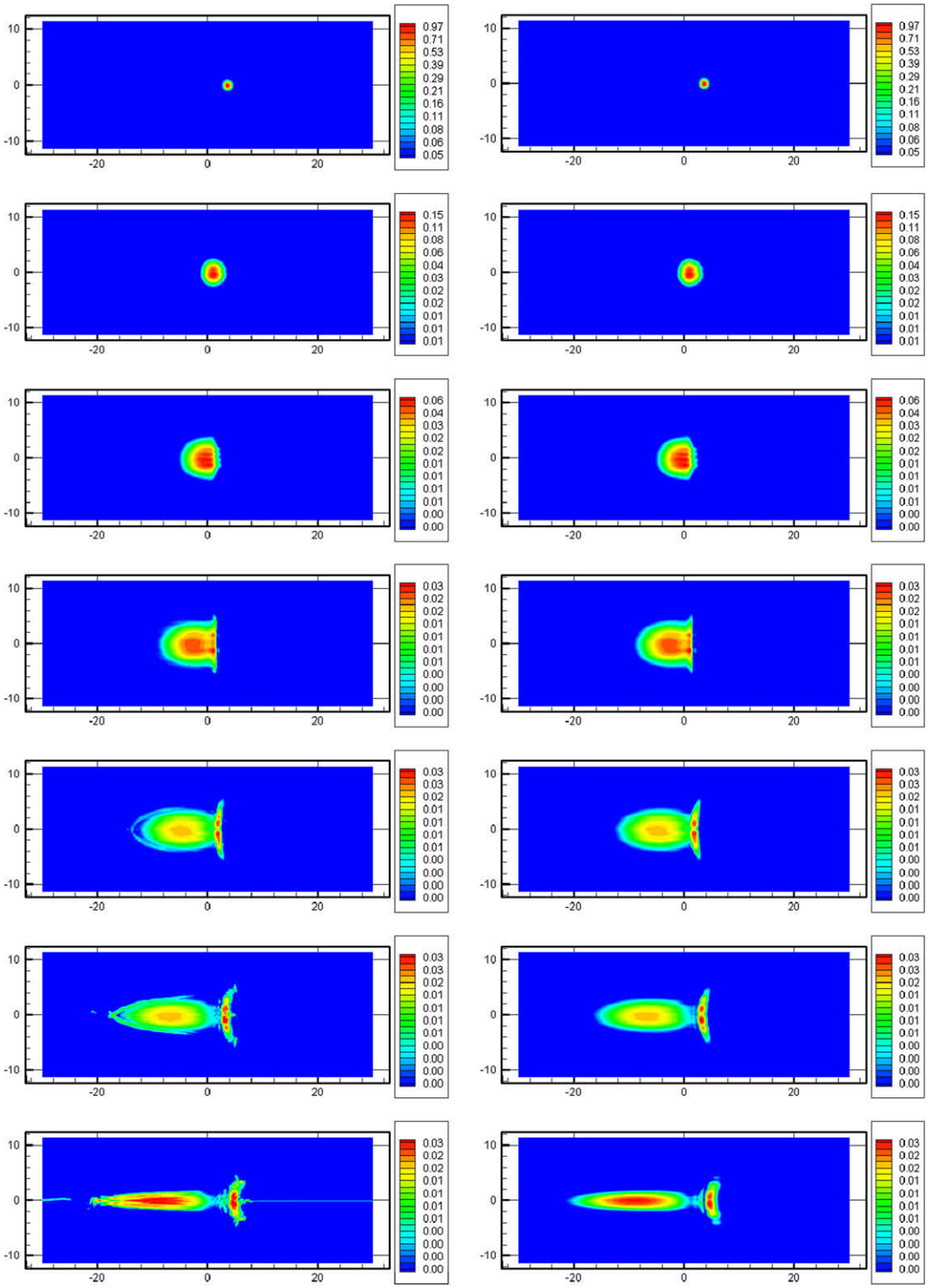

Fig. 10. The amplitude of probability density and the quantum force obtained from the minimum setup probability density using the numerical simulation. (a) $\rho = 10^{-5}$ and (b) $\rho = 10^{-12}$ 2D wave packet motion with downhill ramp potential.

mum setup probability density using the numerical scheme. The change in the quantum potential in Fig. 9b1 exceeds that in Fig. 9a1, because the minimum density in Fig. 9b1 is smaller than that in Fig. 9a1. However, the variation in the effect of the

Table 4
Parameters of QFD simulation for double-slit jet.

b (slit width)	100 nm
ħ (plank constant reduced)	1.055×10^{-34} (Js)
T_0	0.0242 (fs)
m (electron mass)	1 (a.u) = 9.109×10^{-31} kg
$\bar{u}_0$ (initial velocity)	0.013831, 0.027662, 0.041494, 0.055325, 0.069157, 0.1383 (N = 10, 20, 30, 40, 50, 100)
v_0 (initial velocity)	0
$d\bar{x}$	0.03
$d\bar{y}$	0.03
$d\tau$	0.001–0.01 (for various N)

Characteristic velocity = $b/(\pi T_0)$.
All units are atomic unit (a.u.) (1 a.u. = 0.0242 fs); 1 eV = 1.602×10^{-19} J; $a_0 = 0.529 \times 10^{-10}$ m.

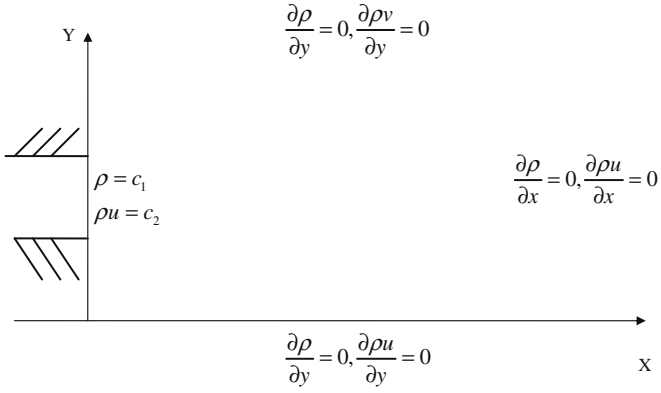

Fig. 11. Boundary conditions for probability density and momentum flux. ρ, ρu, ρv.

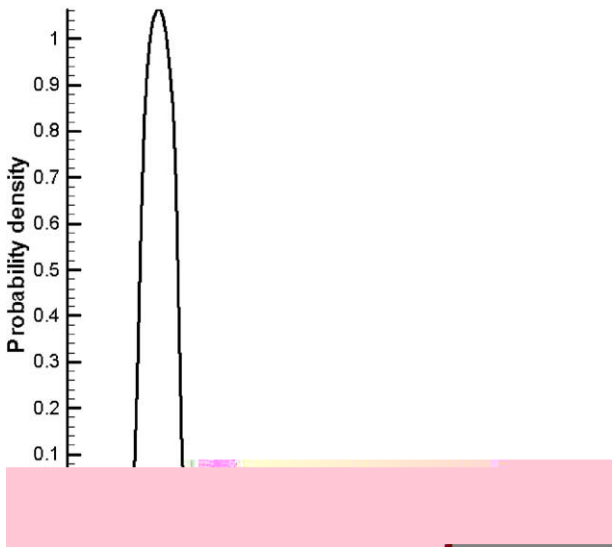

Fig. 12. Probability density and momentum flux distribution at $x = 0.0$ use in numerical simulation.

quantum force is very small. When the minimum density is set to 10^{-5} or 10^{-12} herein, from the red line of the Fig. 9, the wave propagation of probability density maintain stable, indicating the scheme proposed herein can be adopted successfully the variation in value associated caused by potential energy.

Fig. 10 plots the amplitude contours of probability density for two-dimensional free particle motion in downhill ramp potential. This advantage can reduce the calculation error that is caused by the regridding algorithm in the ALE frame.

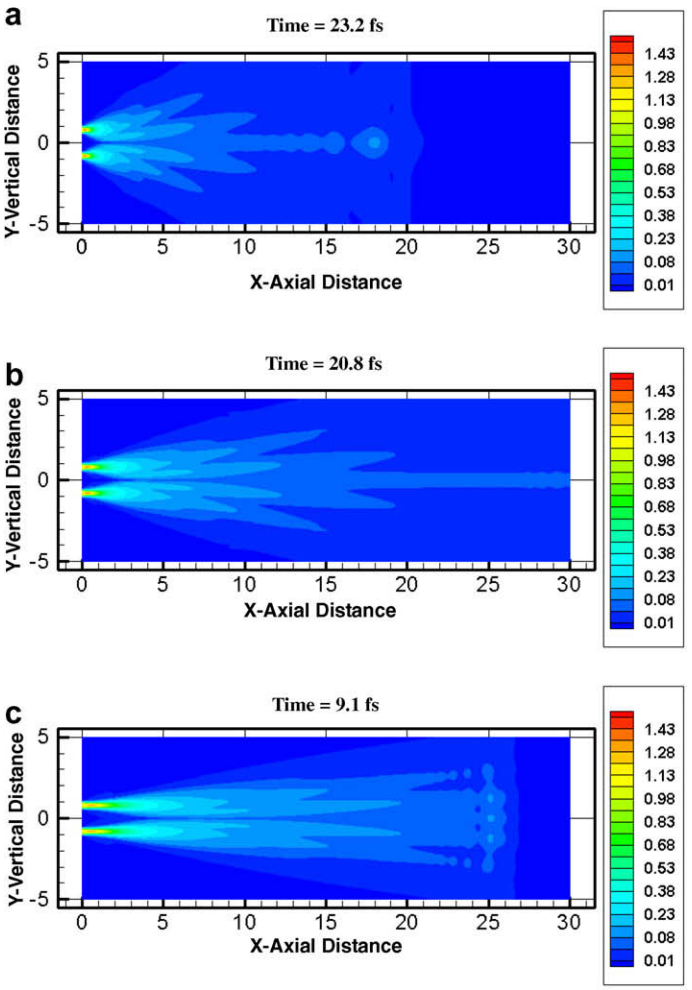

Fig. 13. (a) Contour of probability density for $N = 10$ obtained by QFD simulation at time = 23.2 fs. (b) Contour of the probability density for $N = 30$ obtained by QFD simulation at time = 20.8 fs. (c) Contour of probability density for $N = 50$ obtained by QFD simulation at time = 9.1 fs. (d) Contour of probability density for $N = 60$ obtained by QFD simulation at time = 8.47 fs. (e) Contour of probability density for $N = 100$ obtained by QFD simulation at time = 4.69 fs. (f) Contour of probability density for $N = 200$ obtained by QFD simulation at time = 2.52 fs.

C. Double-slit jet

Quantum mechanics among the nano technology community has received increasing interest in recent years [30]. Quantum nanojets of atoms, molecules, or charged particles are anticipated to have new and important roles in nano-engineering [8–10,30,31]. The structural and dynamic variations of the jets are very complex. Such nanojets must be numerically simulated for some applications with complex boundary conditions and an external potential. In this section, solutions for double-slit jets are obtained using numerical approaches to investigate the nature of structural and dynamic variations of the nanojets in terms of quantum Reynolds number.

To obtain a solution for the two-dimensional two-slit quantum nanojet, the following reference quantities are treated as characteristic quantities of interest

$$\bar{x} = \frac{x}{b/\pi}, \quad \bar{y} = \frac{y}{b/\pi}, \quad \tau = \frac{t}{T_0}, \quad \bar{u} = \frac{u}{U}, \quad \bar{v} = \frac{v}{U}, \quad U = \frac{b/\pi}{T_0}$$

where T_0 is a characteristic time, b is half the distance between slits. U is the characteristic velocity, $\hbar/km_e$. Table 4 presents the parameters of QFD simulation.

In this system of reduced units the continuity equation, and the equations for the x- and y- components of momentum, respectively, become

$$\frac{\partial \rho}{\partial \tau} + \frac{\partial \rho \bar{u}}{\partial \bar{x}} + \frac{\partial \rho \bar{v}}{\partial \bar{y}} = 0 \tag{43}$$

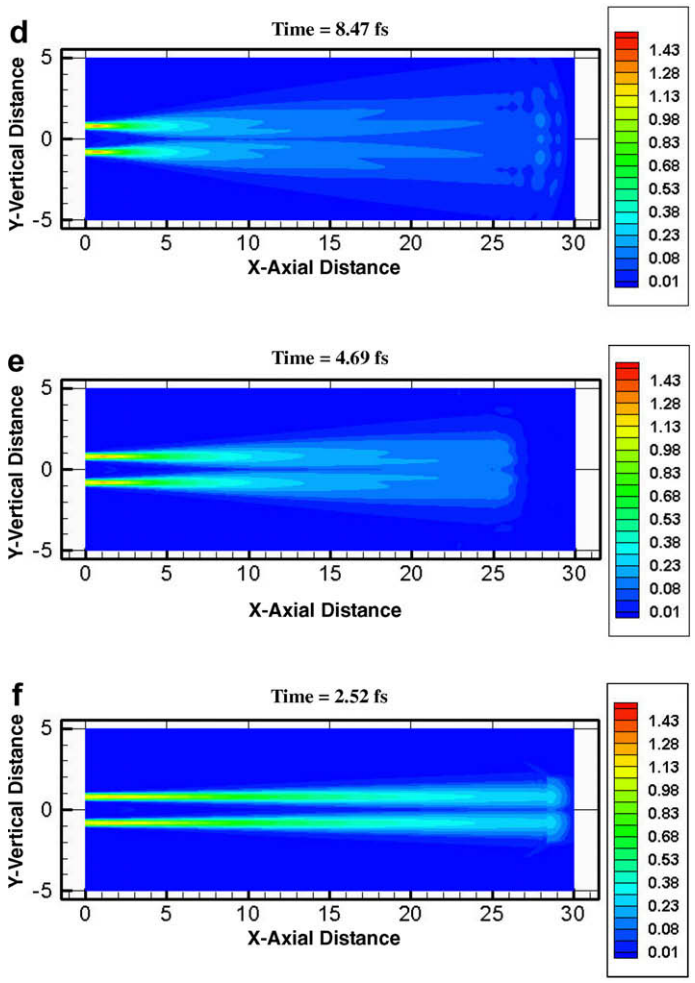

Fig. 13. (*continued*)

$$\frac{\partial \rho \bar{u}}{\partial \tau} + \frac{\partial (\rho \bar{u}^2)}{\partial \bar{x}} + \frac{\partial (\rho \overline{u v})}{\partial \bar{y}} - \frac{1}{2N^2} \rho \frac{\partial}{\partial \bar{x}} \left[\rho^{-1/2} \left(\frac{\partial^2 \rho^{1/2}}{\partial \bar{x}^2} + \frac{\partial^2 \rho^{1/2}}{\partial \bar{y}^2} \right) \right] = 0 \tag{44}$$

$$\frac{\partial \rho \bar{v}}{\partial \tau} + \frac{\partial (\rho \overline{u v})}{\partial \bar{x}} + \frac{\partial (\rho \bar{v}^2)}{\partial \bar{y}} - \frac{1}{2N^2} \rho \frac{\partial}{\partial \bar{y}} \left[\rho^{-1/2} \left(\frac{\partial^2 \rho^{1/2}}{\partial \bar{x}^2} + \frac{\partial^2 \rho^{1/2}}{\partial \bar{y}^2} \right) \right] = 0 \tag{45}$$

where N is quantum Reynolds number

$$N^2 = \frac{2 m_e E}{h^2} \frac{b^2}{\pi^2} = \left(\frac{m_e^2 U^2}{h^2} \frac{b^2}{\pi^2} \right) \tag{46}$$

The boundary conditions at the exit of the quantum nanojet ($x = 0$) are given as

$$\rho(0, \bar{y}) = \begin{cases} \rho_0 & 0.6 \leqslant \bar{y} \leqslant 1.0 \\ 0 & \text{otherwise} \end{cases} \tag{47}$$

$$\bar{u}(0, \bar{y}) = \begin{cases} \bar{u}_0 & 0.6 \leqslant \bar{y} \leqslant 1.0 \\ 0 & \text{otherwise} \end{cases} \tag{48}$$

$$\bar{v}(0, \bar{y}) = 0, \quad y > 0 \tag{49}$$

Figs. 11 and 12 present the boundary conditions and the probability density distribution at $x = 0.0$.

Fig. 13 plots a series of contour map of the probability density for various values of N. Fig. 14 shows the contour probability density for $N = 10$, 50, 100. The contour results reveal small differences between the results obtained using

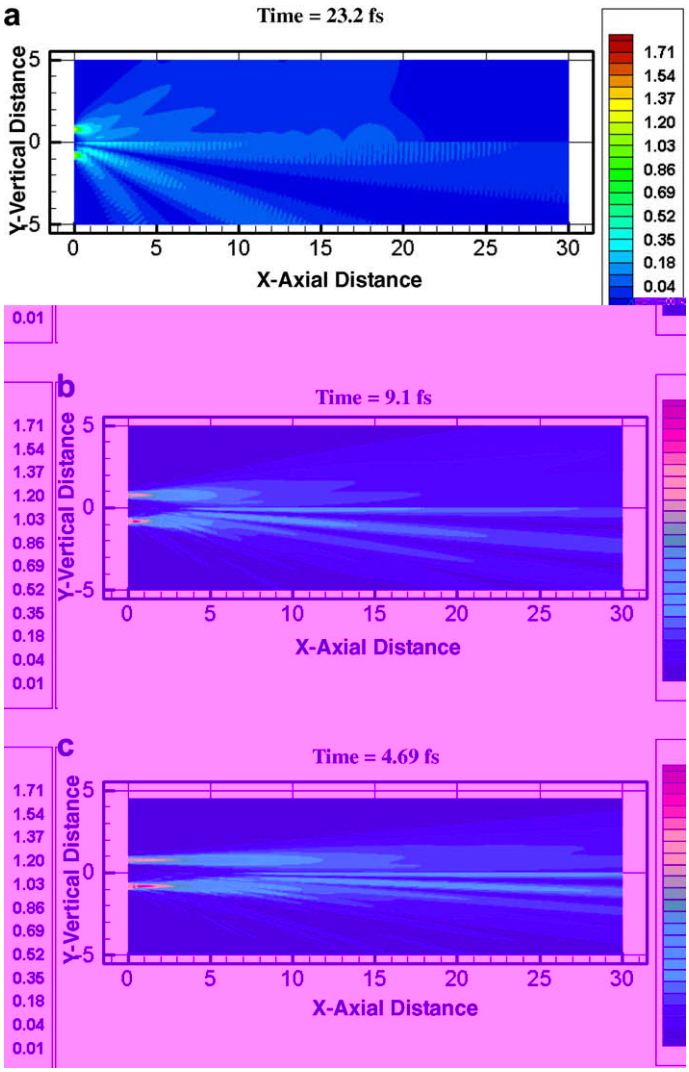

Fig. 14. Contours of probability density for (a) $N = 10$, (b) $N = 50$ and (c) $N = 100$ obtained from QFD solution and analysis at time = 23.2 fs, 9.1 fs, and 4.69 fs.

the analytical and numerical methods. These differences arise simply because the boundary conditions on the probability density distributions are not exactly equal. In the analytical approach a step function is used as the probability density distribution at $x = 0$, and in the QFD simulation, a Gaussian distribution is adopted (Fig. 12). Accordingly, the velocity in the y-direction is smaller near the exit jet and the branching angle is smaller in the QFD simulation.

5. Conclusions

This work presents a novel method for solving quantum hydrodynamic equations of motion. The proposed scheme is based on a control volume technique and the monotone upwind-centered schemes for conservation laws (MUSCL) method is adopted to interpolate the changes in cell properties that occur during flow simulation. As nodes begin to form in the reflected part of the wave package, the quantum potential and force become large and numerical instabilities can arise. A third-order modified Osher–Chakravarthy (MOC) upwind scheme was introduced to obtain the convective terms of the hydrodynamic equations and a second-order central finite volume scheme was used to map the quantum potential field. The scheme successfully prevents the numerical instabilities that are associated with node formation and enables the stable propagation of the wave packet for very long times. The numerical results agree closely with theoretical and other numerical solutions.

The proposed method was applied to a one- and two-dimensional wave packet from a repulsive Eckart barrier and a downhill ramp potential. This problem is intractable using the de Broglie–Bohm formulation of quantum mechanics. The results computed using this approach excellently with those computed using the Crank–Nicholson approach. The accuracy of

the wave function was also investigated. A significant result of these calculations is the stable and unitary propagation of the wave packet fro very long times. Additionally, this numerical technique to quantum-slit jets applied to more application. The presented numerical scheme is highly accurate both temporally and spatially and can solve problems of the quantum hydrodynamic motion.

The de Broglie–Bohm approach is a highly attractive means of solving quantum mechanical problems. However, the intrinsic numerical difficulties associated with this approach must be overcome. The results herein the external potential battier are encouraging and all of the adopted herein are applicable to higher dimensions. Results of this study contribute to efforts to yield a computationally efficient method for treating unclear motion in chemical reactions that involve many atoms.

Acknowledgment

The author acknowledges the support provided by the National Science Council ROC under the Grant NSC-95-2221-E-432-002. Ted Knoy is appreciated for his editorial assistance.

References

[1] D. Bohm, A suggested interpretation of the quantum theory in terms of hidden variables I, Phys. Rev. 85 (1952) 166.
[2] D. Bohm, A suggested interpretation of the quantum theory in terms of hidden variables II, Phys. Rev. 85 (1952) 180.
[3] D. Bohm, Proof that probability density approaches in causal interpretation of the quantum theory, Phys. Rev. 89 (2) (1953) 458–466.
[4] J.H. Weiner, A. Askar, Time-dependent perturbation calculations based on the hydrodynamic analogy to quantum mechanics, J. Chem. Phys. 54 (3) (1971) 1108–1113.
[5] J.H. Weiner, A. Askar, Particle method for the numerical solution of the time-dependent Schrödinger equation, 1971;54(8):3534–3541.
[6] H.H. Chiu, Quantum fluid dynamics and computational quantum fluid dynamics. The 9th National Computational Fluid Dynamics Conference, Tainan, Taiwan, 2002, pp. 30–48.
[7] H.H. Chiu, Quantum modal balance theory and the origin of quantized energy of an atom, in: Proceedings of the Royal Society A: Mathematical, Physical and Engineering Sciences, vol. 461, 2005, pp. 3023–3057.
[8] H.H. Chiu, C.T. Lin, S.Y. Lin, T.C. Hung, F.L. Mardarasz, Developments of Quantum Nanojet based Nanodevices, ICEE11, Hilton Head, 2004.
[9] H.H. Chiu, C.T. Lin, Structural and dynamic complexities of nanojets. Air Force Office of Scientific Research/Taiwan Nanoscience Initiative Workshop Maui, 2004.
[10] H.H. Chiu, C.T. Lin, S.Y. Lin, F.L. Madarasz, Quantum nanojet structures: quantum branching and clustering in two-slit electron jets, J. Comput. Theor. Nanosci. 3 (1) (2006) 88–100.
[11] N. Ercolani, R. Montgomery, On the fluid approximation to a nonlinear Schrodinger equation, Phys. Lett. A 180 (1993) 402–408.
[12] R.E. Wyatt, Quantum wave packet dynamics with trajectories: application to reactive scattering, J. Chem. Phys. 111 (1999) 4406–4413.
[13] C.L. Lopreore, R.E. Wyatt, Quantum wave dynamics with Trajectories, Phys. Rev. Lett. 82 (26) (1999) pp–5193.
[14] K.H. Hughes, R.E. Wyatt, Wavepacket dynamics on arbitrary Lagrangian–Eulerian grids: Application to Eckart barrier, Phys. Chem. Chem. Phys. 5 (2003) 3905–3910.
[15] G. Terlecki, N. Grun, W. Scheid, Solution of the time-dependent Schrödinger equation with a trajectory method and application of H+-H scattering, Phys. Lett. A 88 (1982) 33–36.
[16] P. Zimmerer, M.Z. Grun, W. Scheid, Trajectory method for the time-dependent Schrödinger and Thomas–Fermi equations, Comput. Phys. Commun. 63 (1991) 21–27.
[17] R.G. Brook, P.E. Oppenheimer, C.A. Weatherford, I. Banicescu, Z. Jianping, Solving the hydrodynamic formulation of quantum mechanics: a parallel MLS method, Int. J. Quant. Chem. 85 (2001) 263–271.
[18] B.K. Dey, A. Askar, H. Rabitz, Multidimensional wave packet dynamics within the fluid dynamical formulation of the Schrödinger equation, J. Chem. Phys. 109 (1998) 8770–8782.
[19] B.K. Dey, A. Askar, H. Rabitz, Alternating direction implicit technique and quantum evolution within the hydrodynamical formulation of Schrödinger's equation, Chem. Phys. Lett. 297 (1998) 247–256.
[20] F.S. Mayor, A. Askar, H.A. Rabitz, Quantum fluid dynamics in the Lagrangian representation and applications to photodissociation problems, J. Chem. Phys. 111 (6) (1999) 243–2423.
[21] X.G. Hu, T.S. Ho, H. Rabitz, Solution of the quantum fluid dynamical equations with radial basis function interpolation, Phys. Rev. E 61 (5) (2000) 5967–5976.
[22] X.G. Hu, T.S. Ho, H. Rabitz, Multivariate radial basis interpolation for solving quantum fluid dynamical equations, Comput. Math. Appl. 43 (2002) 525–537.
[23] K.K. Brian, A new method for solving the quantum hydrodynamic equations of motion, J. Chem. Phys. 119 (12) (2003) 5805–5817.
[24] B. Van Leer, Toward the ultimate conservative difference Scheme V, a second-order sequel to Godunov's scheme, J. Comput. 32 (1979) 101–136.
[25] S. Osher, S. Chakravarthy, Very high order accurate TVD schemes. ICASE Report, No. 84-144, 1984, pp. 229–274 (also The IMA Volumes in Mathematics and its Applications, vol. 2, Springer-Verlag, 1985).
[26] P.L. Roe, Approximate Riemann solvers, parameter vectors and difference schemes, J. Comput. Phys. 43 (2) (1981) 357–372.
[27] S.Y. Lin, T.M. Wu, Y.S. Chiu, An upwind finite-volume scheme with a triangular mesh for conservation laws, J. Comput. Phys. 107 (2) (1993) 324–337.
[28] S. Gottlieb, C.W. Shu, Total-variation-diminishing Runge–Kutta schemes, Math. Comput. 67 (1998) 73–85.
[29] N. Zettili, Quantum Mechanics, Concepts and Application, John Wiley and Sons, Inc., New York, 2001.
[30] C. Philippidis, D. Bohm, R.D. Kayes, The Aharonov–Bohm effect and the quantum potential, Nuovo Cimento 71B (1982) 75–88.
[31] C.T. Lin, H.H. Chiu, Structural and dynamic complexities of nanojets", Air Force Office of Scientific Research/Taiwan Nanoscience Initiative Workshop, Maui, 2004.